NDT&E International 139 (2023) 102902

Contents lists available at ScienceDirect

NDT and E International

journal homepage: www.elsevier.com/locate/ndteint

Differentiate tensor low rank soft decomposition in thermography defect detection

Xuran Zhang [a], Bin Gao [a,*], Tongle Wu [a], Wai Lok Woo [b], Junling Fan [c], Shaozheng Zhan [c]

[a] School of Automation Engineering, University of Electronic Science and Technology of China, China
[b] Department of Computer and Information Sciences, Northumbria University, England, UK
[c] Aircraft Strength Research Institute, Xi'An, 710065, China

ARTICLE INFO

Keywords:
Optical pulsed thermography
Tensor decomposition
Thermography defect detection

ABSTRACT

Composites are prone to defects in manufacture , which are to be evaluated for safety through non-destructive testing (NDT) techniques. Thermal images are acquired for NDT by using Optical pulsed thermography. Defect detection can be performed by proposing defect detection algorithms. However, due to the low resolution of defect contrast, the detection performance of the existing algorithm is still sub-optimal. In this work, a decomposition algorithm by differentiating low-rank tensors is proposed to extract weak defect information from complex thermal pattern disturbances for surface and sub-surface defect detection. The algorithm mines deep insight into the information on the differentiation of different ranks between structures from the results of Tucker decomposition to extract defect features. In particular, a probabilistic tensor model is introduced to correct potential mismatch patterns enhance defect contrast, and suppress noise and light spot interference. To verify the effectiveness and robustness of the proposed algorithm, a variety of complex composite specimens have been used for validation. The experimental results show that the proposed algorithm achieves better performance compared to the state-of-the-art algorithms especially in enhancing the defect contrast and suppressing the light spot in seven common samples. In overall, it can provide on average of approximately 15% F-score and 3 dB SNR improvement for validation.

1. Introduction

Tensor based algorithms have attracted wide attention such as in computer vision [1], signal processing [2] , data mining [3]. Cande-Comp/Parafac (CP) and Tucker decomposition [4] are classical algorithms for tensor decomposition. Tucker decomposition is generally designed and solved based on L2 norm. Chachlakis et al. [5] proposed Tucker decomposition based on L1 norm. They presented two solutions based on L1-norm Higher Order Singular Value Decomposition and L1-norm Higher Order Orthogonal Iterations algorithm frameworks. It shows strong corrosion resistance in the processed data. Haddock et al. [6] used CP decomposition in dynamic topic modeling to reduce the interference of noise on detecting potential topics. Liu et al. [7] performed low-rank tensor approximation with CP rank and Tucker rank to complete the estimation of image missing components. Deng et al. [8] proposed an unsupervised anomaly detection method by combining Tucker decomposition with single-class support vector machine, which improved the accuracy and efficiency of performance without destroying data structure. In addition, non-negative tensor decomposition [9] imposes non-negative constraints on the factorization matrix. Veganzones et al. applied the non-negative CP decomposition algorithm based on compression to multi-linear spectral decomposition, and analyzed hyperspectral data tensors such as hyperspectral time series [10]. However, both Tucker and CP decomposition algorithms are required to manually set the rank. To automatically determine the rank, Zhao et al. [11] proposed a hierarchical probability model to formulate CP factorization by adopting complete Bayesian processing and adding sparse priors. In addition to these two basic models, robust principal component analysis (TRPCA) has become one of the important models in the field of tensor decomposition. Lu et al. [12] proposed a new TRPCA algorithm with tensor kernel norm constraint based on tensor singular value decomposition (T-SVD). Jiang et al. [13] replaced the Fourier transform in T-SVD framework with the tight wavelet frame and applied it in tensor robust principal component analysis (TRPCA). Shahid et al. [14] proposed a low-rank sparse tensor decomposition algorithm based on Graph Laplacian regularization. They projected the tensor onto a

* Corresponding author.
E-mail address: bin_gao@uestc.edu.cn (B. Gao).

https://doi.org/10.1016/j.ndteint.2023.102902
Received 4 September 2022; Received in revised form 26 June 2023; Accepted 28 June 2023
Available online 13 July 2023
0963-8695/

low-dimensional graph basis to reduce the computation at the SVD step. Compared with TRPCA, the running time was greatly reduced while maintaining the original effect. Zhou et al. [15] proposed anomalous robust tensor principal component analysis (OR-TRPCA) to restore low-rank tensor and anomaly detection. Bengua et al. [16] proposed a tensor completion algorithm based on the tensor train (TT) rank. They avoided SVD with high computational load by approximating TT rank with a matrix decomposition model, and obtained higher-order representations of low-order tensors through ket augmentation. In these ways, the completion effect and operation efficiency of the algorithm were improved. Meng et al. [17] proposed a novel tensor-based robust principal component analysis (TenRPCA) for enhancing the background difference [18]. Wu et al. [19] proposed a novel hierarchical low-rank and sparse tensor decomposition (HLSTD) to extract micro crack information under the inductive heat image. Tensor decomposition is also used in deep learning. Tjandra et al. [20] compressed the weight matrix in RNN by using Tucker decomposition, CP decomposition and tensor train decomposition algorithms to reduce the number of parameters while maintaining the effect of RNN.

With the continuous development of modern industry, composite materials [21] have been widely used. Due to the influence of manufacturing and fatigue damage, internal defects [22] such as debonds and delaminations inevitably occur in composites. Therefore, non-destructive testing (NDT) [23] of optical pulsed thermography (OPT) [24] has been effectively used in the defect detection of composite materials. Farmaki et al. [25] proposed pulsed phase-informed lock-in thermography for detecting subsurface and superficial damage in aircraft-grade composite materials. In OPT, the temperature of the material is varied by using an external excitation source. The thermography of both defect and non-defect regions can be recorded by a thermal camera for defect detection.

Due to the influence of environmental noise and other unpredictable factors, the thermal images collected by OPT have shortcomings of detection. These include fuzzy edges, low resolution and inconspicuous defect features. Therefore, defect information will be processed by feature extraction algorithms. Several traditional methods of infrared sequential image processing are proposed, including thermal signal reconstruction (TSR) [26], pulsed phase thermal imaging (PPT) [27] and principal component thermal imaging (PCT) [28]. In TSR, the sequence image data in the cooling stage are polynomial fitted in the logarithmic domain. More defect information is obtained by calculating the first and second derivatives of reconstructed image sequences. Leyburn University researchers [26] proposed an algorithm for defect depth prediction by using the maximum second derivative of TSR. Maldague et al. [27] proposed pulse phase thermography (PPT) for defect analysis. PPT extracts the defect information through the difference of the phase and amplitude information between the defect and non-defect regions in the frequency domain. This process improves the detection sensitivity and anti-interference ability. Ishikawa et al. [29] used phase contrast caused by the defect regions when using PPT at a suitable high frequency. In this case, the high visibility of the defect is ensured and the detection time can be shortened. In particular, tensor and matrix decomposition-based works has been employed for thermography processing. Yousefi et al. [30] proposed a faster PCT in order to eliminate the covariance matrix. A shorter computational alternative is used instead of the calculation of covariance matrix. Yousefi et al. [31] proposed semi convex and sparse negative matrix factorization (NMF) to detect abnormal subsurface thermal patterns. Liu et al. [32] proposed using the independent component thermography (ICT) to detect defects in carbon fiber reinforced polymer (CFRP) composites. Independent Component Analysis (ICA) was used to separate the defect signal from the thermal image background with uneven heating. Defects generally occupy a small proportion in the sample and can be considered as sparsely distributed. Therefore, the thermal data of the defect part is taken as the abnormal heat mode image with the sparse property while this part is embedded into the background image of the normal heat mode with the low-rank property. Wu et al. [33] proposed sparse principal component thermography (SPCT) with structural sparsity by combining PCT with the penalization term. Liu et al. [34] proposed a structured iterative alternating sparse matrix decomposition. In the framework of the alternate-direction multipliers, the sparse matrix under the tri-decomposition framework was further decomposed for defect detection by combining with the vertex component analysis (VCA).

In overall, the existing feature extraction algorithms are vulnerable to the interference of background information, light spot, noise and so on. The resolution, contrast and SNR of the detection effects need to be further enhanced. Due to the interference of background light spot and the complex characteristics of the specimen, such as subsurface defect and irregularity, we propose differentiate low rank tensor decomposition algorithm. Contributions can be illustrated as follows:

i Differentiate low rank modelling can effectively suppress noise, and the contrast between defect area and non-defect area can be significantly enhanced in tensor decomposition.
ii The foreground part (defect information) of the image sequence is effectively extracted by using information on differentiate of different rank between structures from the results of Tucker decomposition.
iii Probability tensor modeling is introduced to correct potential mismatch patterns, enhance image contrast and suppress noise information as well as light spot interference.

The remaining of the paper has been organized as follows: The details of the proposed method and the quantitative detectability assessment indicators are described in Section 2. The experiment and result analysis are carried out in Section 3. Conclusion and further work are outlined in Section 4.

2. Methodology

2.1. Proposed model

Let $X \in \mathrm{R}^{H\times W\times T}$ be a third order tensor to represent the thermography sequence data. In the proposed model, we decompose X into three tensors as follows

$$X = L + S + N \tag{1}$$

where $L \in \mathrm{R}^{H\times W\times T}$ is a low-rank tensor corresponding to the background. $S \in \mathrm{R}^{H\times W\times T}$ is a sparse tensor, corresponding to defects information, $N \in \mathrm{R}^{H\times W\times T}$ corresponds to the noise or interference. Part of noise belongs to high frequency noise, which can be removed by wavelet transform. Using the stationary wavelet transform [35], X can be decomposed into an approximation image $Y \in \mathrm{R}^{H\times W\times T}$ and three wavelet sub-band images $H \in \mathrm{R}^{H\times W\times T}$, $V \in \mathrm{R}^{H\times W\times T}$, $D \in \mathrm{R}^{H\times W\times T}$. $N \in \mathrm{R}^{H\times W\times T}$ is expressed as follows:

$$N = N_1 + H + V + D \tag{2}$$

N_1 is the residual noise component after wavelet transform.
Substitute (2) into (1) to obtain (3).

$$X = L + S + N_1 + H + V + D \tag{3}$$

Low-frequency images have been retained by wavelet transform is expressed as formula (4).

$$Y = L + S + N_1 \tag{4}$$

Under this sparse and low-rank decomposition framework, TRPCA is generally used to solve the problem. The specific mathematical model is expressed as

$$\min_{L,S} \|L\|_* + \lambda \|S\|_1, \text{s.t. } Y = L + S \tag{5}$$

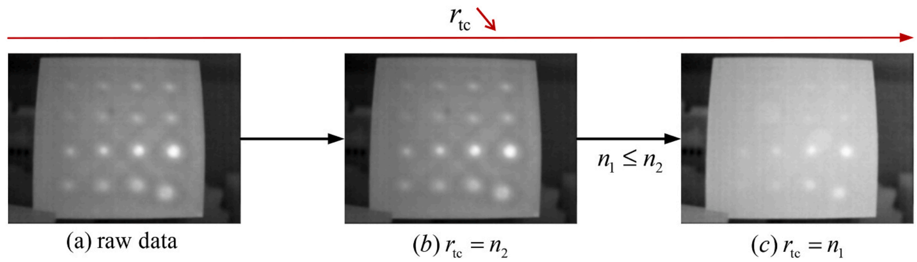

Fig. 1. In the Tucker rank, the first two dimensions ($\mathrm{rank}(Y^{\{i\}})_{i=1,2}$) are set unchanged, while the third dimension (r_{tc}) is changed. the Tucker result obtained is compared with the original image. (a) raw data. (b) Tucker decomposition results images based on $r_{tc} = n_2$. (c) Tucker decomposition results images based on $r_{tc} = n_1$.

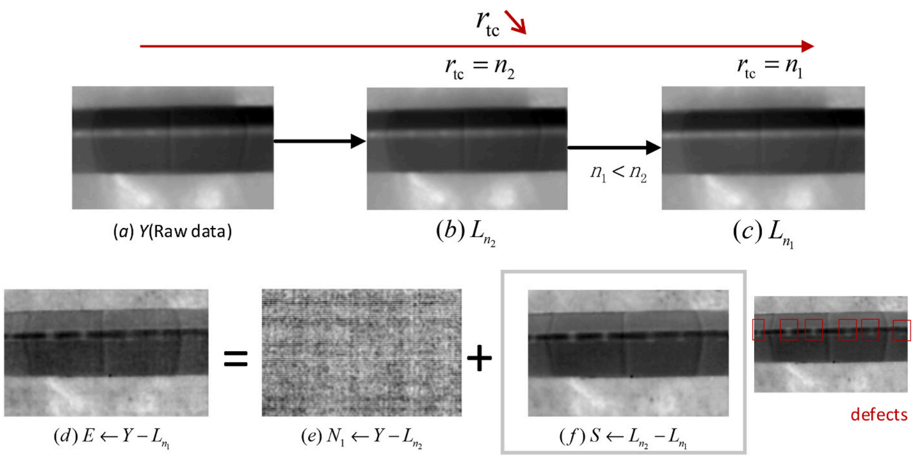

Fig. 2. In the Tucker rank, the first two dimensions ($\mathrm{rank}(Y^{\{i\}})_{i=1,2}$) are set unchanged, while the third dimension (r_{tc}) is changed, and the Tucker result obtained is compared with the original image. (a) raw data (Y). (b) L_{n_2} is Tucker decomposition results images based on $r_{tc} = n_2$. (c) L_{n_1} is Tucker decomposition results images based on $r_{tc} = n_1$. (d) E is the foreground component plus the noise component. (e) N_1 is noise part, the result of $Y - L_{n_3}$. (f) The preliminary foreground result S is the Tucker decomposition result corresponding to rank increment.

where $\|\bullet\|_*$ and $\|\bullet\|_1$ are the low-rank and sparse constraints. However, Y still contains noise and interference, then (5) becomes

$$\min_{L,S} \|L\|_* + \lambda\|S\|_1, \text{s.t. } \|L + S - Y\|_F^2 < \delta \tag{6}$$

where $\|\bullet\|_F$ denotes the extensions of the Frobenius norm on tensors, and $\delta > 0$.

The proposed solution for L and S is not only directly constraining L and S but also using Tucker factorization for approximation. Tucker decomposition is widely used in low rank tensor approximation but it is highly dependent on the rank. Since image is viewed as a matrix, the rank of the matrix determines the amount of information within the image. The rank of the image is low when most of its pixels are similar such as grassland, etc. Once elements different from the background are added, such as a horse or a house, the rank rises. Therefore, with the increase of the rank, the approximate result graph will contain more details in the original image. Usually, the low-rank part of the image is used as its background. We regard a thermography video in which the background is fixed and the foreground varies in time as a tensor Y of the third order along the time dimension. Tucker rank is generally used as

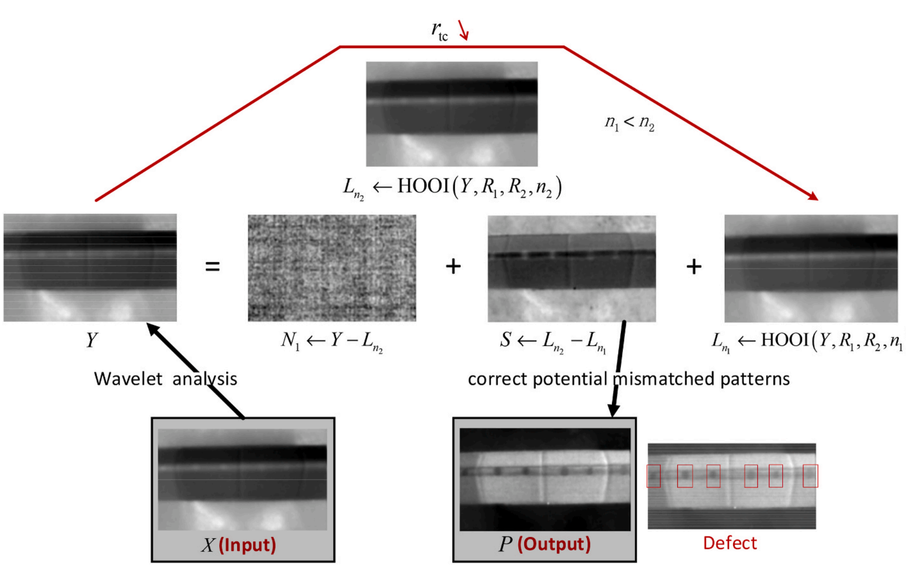

Fig. 3. Framework of the proposed method. X is the raw video sequence. Y is obtained by applying wavelet analysis to X. HOOI(.) indicates Tucker decomposition, detailed see 2.2.1. L_{n_2} is Tucker decomposition results images based on $r_{tc} = n_2$. L_{n_1} is Tucker decomposition results images based on $r_{tc} = n_1$. R_1, R_2, n_1, n_2 are Tucker rank. N_1 is noise part, the result of $Y - L_{n_3}$. The preliminary foreground result S is the Tucker decomposition result corresponding to rank increment. P is the final result, which is calculated by correcting the mismatched patterns in S.

the tensor rank. Tucker rank is a vector, defined as $\mathrm{rank}_{tc}(Y) = (\mathrm{rank}(Y^{\{1\}}), \mathrm{rank}(Y^{\{2\}}), \mathrm{rank}(Y^{\{3\}}))$, where $Y^{\{i\}}$ is the mode-I matricization of Y. The term r_{tc} is the value at $\mathrm{rank}(Y^{\{3\}})$, the integer value between $1 \le r_{tc} \le \mathrm{rank}(Y^{\{3\}})$. Combined with the analysis of the spatial-temporal characteristics of the tensor, a hypothesis is proposed. In the approximation process, specific information in the image can be obtained by changing the value of the third dimension in the Tucker rank of the tensor. Since rank is set as sufficiently small, the low-rank approximation obtained by Tucker decomposition can be regarded as background. As the value of rank increases gradually, the foreground component in the results of Tucker decomposition of approximation will gradually increase. n_1 and n_2 are two different values of rank, and they have been hypothesized as $1 \le n_1 \le n_2 \le \mathrm{rank}(Y^{\{3\}})$. When $r_{tc} = n_1$, the corresponding Tucker decomposition can be modeled as background component. Once $r_{tc} = n_2$, the corresponding Tucker decomposition might contain both background and foreground components. This is shown in Fig. 1 for an intuitive illustration.

Therefore, we can assume that as long as an appropriate rank increment is found, the incremental component of the corresponding Tucker decomposition can be approximated as the foreground component. Fig. 2 provides an intuitive illustration. When the appropriate n_1 and n_2 are selected, the foreground (defects)can be effectively extracted.

Generally, the noise exists in the highest rank component of the tensor as a large number of abrupt and irregular small components. The advantage of using Tucker decomposition when $r_{tc} = n_2$ instead of using the original image can be drawn that the noise can be significantly removed. However, although the Tucker decomposition results in these two ranks have similar patterns, partial patterns may not match through direct subtraction in which hinders extraction of the foreground. Thus, we propose to add weights P to correct the potential mismatched patterns. $P \in \mathrm{R}^{H\times W\times T}$ is set as a probability tensor in which represents the probability that each pixel position of the resulting image sequence S is not the foreground. It is worth noting that automatically learning P is required. In conjunction with P, we assume that the probability distribution that best represents the current state of knowledge is the probability distribution of the prior data with maximum entropy. Fig. 3 illustrates the strategy framework of the proposed method.

2.2. Differentiate tensor decomposition model

Combined with the above analysis, the proposed objective function can be modeled as :

$$\begin{aligned}
&\min_{P} \frac{1}{2}\left\|\sqrt{P}\odot S\right\|_F^2 + \alpha\|\widehat{P}\|_1 + \beta\sum_{w=1}^{W}\sum_{h=1}^{H}\sum_{t=1}^{T} p_{wht}\lg p_{wht} + \widehat{p}_{wht}\lg\widehat{p}_{wht} \\
&s.t.\ \ P + \widehat{P} = 1, p_{wht}\in[0,1] \\
&L_{n_2} = L_{n_1} + S \\
&L_{n_2} = \min_{r_{tc}\le n_2}\|L_{n_2} - Y\| \\
&L_{n_1} = \min_{r_{tc}\le n_1}\|L_{n_1} - Y\|
\end{aligned} \tag{7}$$

The parameter α and β in the formula are the regularization coefficient. $\widehat{P} \in \mathrm{R}^{H\times W\times T}$, as a probability tensor, represents the probability whether each pixel position of the resulting image sequence S belong to the foreground. $\|\bullet\|_F^2$ and $\|\bullet\|_1$ correspond to the L1 norm and the F norm, respectively. Where $\|\bullet\|$ denote the tensor norm. The background tensor $L_{n_1} \in \mathrm{R}^{H\times W\times T}$ is solved by Tucker decomposition based on $r_{tc} \le n_1$. $L_{n_2} \in \mathrm{R}^{H\times W\times T}$ is solved by Tucker decomposition based on $r_{tc} \le n_2$. The foreground tensor S is the incremental component of the Tucker decomposition result when the rank changes from n_1 to n_2, namely difference of $L_{n_2} - L_{n_1}$.

The entry values of S are distributed differently in the foreground and background regions. When pixel value at the foreground is set higher, this results in a larger weight constraint at the foreground P in the first optimization item, and a smaller entry value (probability) in P. This behaves consistent with our interpretation of P. The foreground is sparsely distributed in the image while the value of most items in P is close to 0. We use the L1 norm to constrains P. Finally, the last constraint in the optimization function is set according to the maximum entropy principle.

We solve the above problems in the following steps.

$$\begin{aligned}
&L_{n_1} \leftarrow \min_{r_{tc}\le n_1}\|L_{n_1} - Y\| \\
&L_{n_2} \leftarrow \min_{r_{tc}\le n_2}\|L_{n_2} - Y\| \\
&S \leftarrow L_{n_2} - L_{n_1} \\
&P \leftarrow \frac{1}{2}\min_{P}\left\|\sqrt{P}\odot S\right\|_F^2 + \alpha\|\widehat{P}\|_1 + \beta\sum_{w=1}^{W}\sum_{h=1}^{H}\sum_{t=1}^{T} p_{wht}\lg p_{wht} + \widehat{p}_{wht}\lg\widehat{p}_{wht} \\
&s.t.\ \ P + \widehat{P} = 1, p_{wht}\in[0,1]
\end{aligned} \tag{8}$$

2.2.1. Tucker decomposition

There are several common solution methods for Tucker decomposition, such as HOSVD, BCD and HOOI algorithm. The HOOI algorithm is adopted in this paper. Tucker decomposition decomposes a tensor $Y \in \mathrm{R}^{H\times W\times T}$ into a core tensor multiplied (or transformed) by a matrix along each mode. The core tensor $G \in \mathrm{R}^{H\times W\times T}$ and orthogonal factor matrix $\mathbf{A}^{(1)} \in \mathrm{R}^{H\times R_1}$, $\mathbf{A}^{(2)} \in \mathrm{R}^{W\times R_2}$ and $\mathbf{A}^{(3)} \in \mathrm{R}^{T\times R_3}$ are obtained through calculation by Tucker decomposition. The result of multiplying G with different factor matrices in different modes is approximate to the original data tensor Y. Thus, we have

$$Y \approx G\times_1\mathbf{A}^{(1)}\times_2\mathbf{A}^{(2)}\times_3\mathbf{A}^{(3)} = \sum_{r_1=1}^{R_1}\sum_{r_2=1}^{R_2}\sum_{r_3=1}^{R_3} g_{r_1r_2r_3}a_{r_1}^{(1)}\circ a_{r_2}^{(2)}\circ a_{r_3}^{(3)} \tag{9}$$

$\mathbf{A}^{(1)}$, $\mathbf{A}^{(2)}$ and $\mathbf{A}^{(3)}$ are the main components of 1,2 and 3 modes respectively, and R_1, R_2 and R_3 correspond the Tucker ranks, $\mathrm{rank}_{tc}(Y) = (R_1, R_2, R_3)$. $a_{r_1}^{(1)}$, $a_{r_2}^{(2)}$, $a_{r_3}^{(3)}$ are the r_1th, r_2th, r_3th columns of the matrices $\mathbf{A}^{(1)}$, $\mathbf{A}^{(2)}$ and $\mathbf{A}^{(3)}$. $g_{r_1r_2r_3}$, as an element of G corresponds the level of interaction between the different components. The symbol "$\circ$" corresponds the vector outer product and $\times_n (n = 1, 2, 3)$ denotes the tensor n-mode product.

With above, the optimization problem can be solved as

$$\min_{G,\mathbf{A},\mathbf{B},\mathbf{C}}\left\|Y - G\times_1\mathbf{A}^{(1)}\times_2\mathbf{A}^{(2)}\times_3\mathbf{A}^{(3)}\right\| \tag{10}$$

where the solution is subject to $G \in \mathrm{R}^{H\times W\times T}$, and $\mathbf{A}^{(1)}$, $\mathbf{A}^{(2)}$ and $\mathbf{A}^{(3)}$ are column-wise orthogonal. The objective function is rewritten in vectorized form as

$$\left\|\mathrm{vec}(Y) - \left(\mathbf{A}^{(1)}\otimes\mathbf{A}^{(2)}\otimes\mathbf{A}^{(3)}\right)\mathrm{vec}(G)\right\| \tag{11}$$

It is obvious that G must satisfy the following expression

$$G = Y\times_1{\mathbf{A}^{(1)}}^{\mathrm{T}}\times_2{\mathbf{A}^{(3)}}^{\mathrm{T}}\times_3{\mathbf{A}^{(3)}}^{\mathrm{T}} \tag{12}$$

Then the squared of the object function is rewritten as

$$\|Y\|^2 - \left\|Y\times_1{\mathbf{A}^{(1)}}^{\mathrm{T}}\times_2{\mathbf{A}^{(2)}}^{\mathrm{T}}\times_3{\mathbf{A}^{(3)}}^{\mathrm{T}}\right\|^2 \tag{13}$$

Since $\|Y\|^2$ is constant, we redescribe the objective function as the following maximization problem.

$$\max_{\mathbf{A}^{(n)}}\left\|Y\times_1{\mathbf{A}^{(1)}}^{\mathrm{T}}\times_2{\mathbf{A}^{(2)}}^{\mathrm{T}}\times_3{\mathbf{A}^{(3)}}^{\mathrm{T}}\right\| \tag{14}$$

where $\mathbf{A}^{(n)}$ subject to column-wise orthogonal for $n = 1, 2, 3$.The objective function in (14) can be rewritten in matrix form as

Table 1
Tucker decomposition: HOOI(Y, R_1, R_2, R_3).

Input: original data Y, Tucker rank R_1, R_2, R_3
Output: L
Initialize: $\mathbf{A}^{(n)}$ for $n = 1, 2, 3$ using HOSVD
Repeat
  For $n = 1, 2, 3$ do
    $\mathbf{Z} \leftarrow Y \times_1 \mathbf{A}^{(1)\mathrm{T}} \cdots \times_{n-1} \mathbf{A}^{(n-1)\mathrm{T}} \times_{n+1} \mathbf{A}^{(n+1)\mathrm{T}} \cdots \times_3 \mathbf{A}^{(3)\mathrm{T}}$
    $\mathbf{A}^{(n)} \leftarrow R_n$ leading left singular value vector of $\mathbf{Z}_{(n)}$
  End for
Until fit ceases to improve or maximum iterations exhausted
$G \leftarrow Y \times_1 \mathbf{A}^{(1)^{\mathrm{T}}} \times_2 \mathbf{A}^{(3)^{\mathrm{T}}} \times_3 \mathbf{A}^{(3)^{\mathrm{T}}}$
Return $L = G \times_1 \mathbf{A}^{(1)} \times_2 \mathbf{A}^{(2)} \times_3 \mathbf{A}^{(3)}$

$$\left\|\mathbf{A}^{(n)^{\mathrm{T}}}\mathbf{Z}\right\| \quad \mathbf{Z} = \mathbf{Y}_{(n)}\left(\mathbf{A}^{(3)} \otimes \cdots \otimes \mathbf{A}^{(n+1)} \otimes \mathbf{A}^{(n-1)} \otimes \cdots \otimes \mathbf{A}^{(1)}\right) \tag{15}$$

where $\mathbf{A}^{(n)}$ is obtained by taking the R_n in leading left singular value vector of $\mathbf{Z}$ by SVD. We then use HOSVD as the starting point for the iterative algorithm. More detailed information can be found in Ref. [36]. Thus, the optimization processes of algorithm can be summarized in Table 1. In this algorithm, the singular value decomposition (SVD) is used and rank n determines the number of components to be intercepted. Therefore, the Tucker decomposition results the components of the rank increment, can be approximately regarded as the extraction of $n_2 - n_1$ components. As long as the appropriate rank is found, the component corresponding to the foreground can be extracted.

2.3. Solving the tensor P

$$P \leftarrow \frac{1}{2}\min_{P}\left\|\sqrt{P} \odot S\right\|_{\mathrm{F}}^2 + \alpha\|\widehat{P}\|_1 + \beta\sum_{w=1}^{W}\sum_{h=1}^{H}\sum_{t=1}^{T} p_{wht}\,\lg p_{wht} + \widehat{p}_{wht}\,\lg\widehat{p}_{wht}$$
$$s.t.\ \ P + \widehat{P} = 1, p_{wht} \in [0, 1] \tag{16}$$

Optimizing the entry value of P separately, formula (16) is equivalent to formula (17).

$$\min_{p_{wht}}\frac{1}{2}\left\|\sqrt{p_{wht}} \odot s_{wht}\right\|_{\mathrm{F}}^2 + \alpha\|\widehat{p}_{wht}\|_1 + \beta(p_{wht}\,\lg p_{wht} + \widehat{p}_{wht}\,\lg\widehat{p}_{wht})$$
$$s.t.\ \ p_{wht} + \widehat{p}_{wht} = 1, p_{wht} \in [0, 1]\forall w, h, t \tag{17}$$

By Lagrange function method, the equation constraint is formula (18).

$$\begin{aligned}\mathrm{L}(p_{wht}, \widehat{p}_{wht}, m_{wht}) = &\frac{1}{2}p_{wht}s_{wht}^2 + \alpha\widehat{p}_{wht} + \beta(p_{wht}\,\lg p_{wht} + \widehat{p}_{wht}\,\lg\widehat{p}_{wht})\\ &+ m_{wht}(p_{wht} + \widehat{p}_{wht} - 1)\end{aligned} \tag{18}$$

where M is Lagrange multiplier. Solve the partial derivative of each variable and set it to zero.

$$\begin{aligned}&\frac{\partial\mathrm{L}}{\partial p_{wht}} = \frac{1}{2}s_{wht}^2 + \beta + \beta\,\lg p_{wht} + m_{wht} = 0\\ &\frac{\partial\mathrm{L}}{\partial\widehat{p}_{wht}} = \alpha + \beta + \beta\,\lg\widehat{p}_{wht} + m_{wht} = 0\\ &\frac{\partial\mathrm{L}}{\partial m_{wht}} = p_{wht} + \widehat{p}_{wht} - 1 = 0\end{aligned} \tag{19}$$

p_{wht} has a closed solution.

$$p_{wht} = \frac{\exp^{-\frac{s_{wht}^2}{2\beta}}}{\exp^{-\frac{s_{wht}^2}{2\beta}} + \exp^{-\frac{\alpha}{\beta}}} \tag{20}$$

p_{wht} is like sigmod function which normalized in [0,1]. This is consistent with the classification probability interpretation of P.

The optimization processes of the proposed algorithm can be summarized in Table 2.

Table 2
Proposed algorithm.

Input: original data Y, Tucker rank R_1, R_2, n_1, n_2
Output: foreground tensor P
$L_{n_1} = \mathrm{HOOI}(Y, R_1, R_2, n_1)$
$L_{n_2} = \mathrm{HOOI}(Y, R_1, R_2, n_2)$
$S = L_{n_2} - L_{n_1}$
$P \leftarrow p_{wht} = \dfrac{\exp^{-\frac{s_{wht}^2}{2\beta}}}{\exp^{-\frac{s_{wht}^2}{2\beta}} + \exp^{-\frac{\alpha}{\beta}}}$
Return P

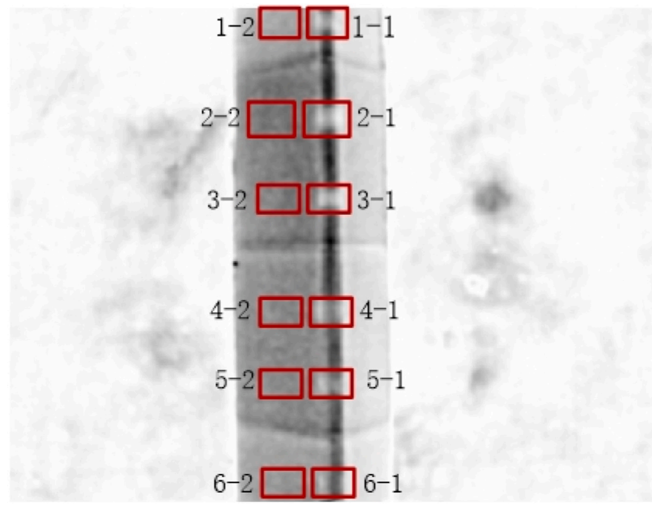

Fig. 4. Schematic diagram of SNR calculation.

2.4. Quantitative detectability assessment

Two merit factors were selected to evaluate the defect detection ability of the proposed algorithm. SNR was used to evaluate the contrast between defect and non-defect areas of the experimental results. F-Score was used to evaluate the defect detection accuracy of the algorithm.

SNR is expressed as follows:

$$SNR = 20\,\lg\left(\frac{T_d}{T_{non}}\right) \tag{21}$$

where T_d denotes the sum of pixel values in the selected defect area, and T_{non} denotes the sum of pixel values in the corresponding non-defect area. The unit is decibel (dB). In our paper, when we maximize the SNR, we are essentially jointly maximizing the signal term (S) and minimizing the noise term (N). The noise term includes both sensor noise and background of the image. In practical term, when an image is captured by a recording device, the sensor noise is also being captured. Thus, the background of a captured image has contained the sensor noise as well as other background artefacts.

In the calculation of indicators, a defect area is selected as a prior information for the calculation of T_d, as shown in Fig. 4. 1-1 area. Meanwhile, the area with the same size as the selected defect area was selected in the adjacent area for the calculation of T_{non}, as shown in Fig. 4. 1–2 area. When the SNR of an image is calculated, the mean value of the absolute value of the SNR of all defects is taken.

F-score is expressed as follows:

$$F - score = \frac{(\beta^2 + 1)(Precision \times Recall)}{(\beta^2 \times Precision) + Recall} \tag{22}$$

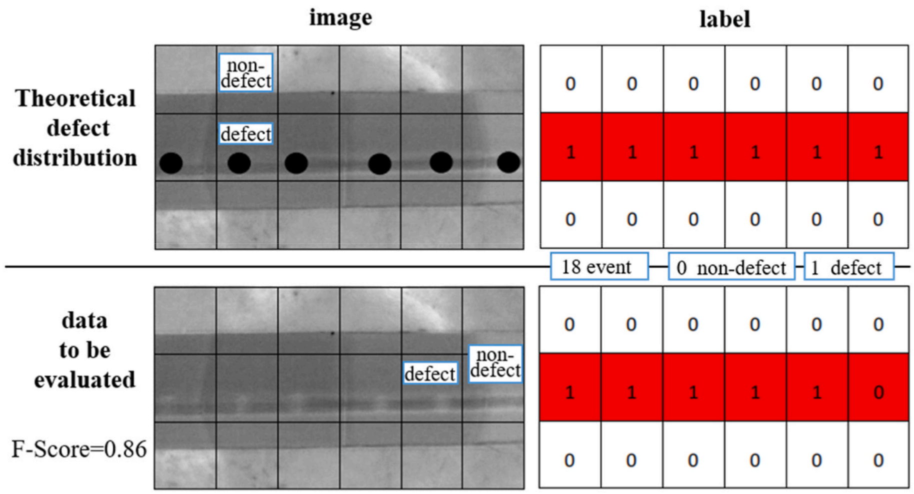

Fig. 5. Schematic diagram of F-Score calculation.

(a) (b)

Fig. 6. Experimental system diagram (a) the portable photoexcited thermal imaging system. (b) the 2000W photoexcited infrared thermal imaging system.

Precision , *Recall* are expressed as follows.:

$$Precision = \frac{TP}{TP + FP} \tag{23}$$

$$Recall = \frac{TP}{TP + FN} \tag{24}$$

Since Precision and Recall rates show opposite trends, β is used to define the importance of the two indicators. The detection task needs to detect all defects where the impact of missed detection (FN) is more serious than that of false detection (FP). Recall has a greater impact for detection. After experimental verification, β is set to 2. The grid method is used to facilitate the statistics of defect and non-defect areas. Fig. 5 shows an approach to statistics using the grid approach. The image is divided into a grid of 3×6. Each grid is treated as an event with defective or non-defective attributes. The real sample at the top of the figure provides reference calculation for the sample to be evaluated at the bottom. The black circles in the figure represent the theoretical defects. The table on the right represents the distribution of defects in the image on the left. In the table, 0 represents the non-defect area and 1 represents the defect area. According to statistics, there are 12 non-defect and 6 defect regions in the real sample, and 13 non-defect and 5 defect regions in the sample to be evaluated. TP is 5, FP is 0, and FN is 1. According to the calculation, F-score is 0.86.

3. Experiment and result analysis

3.1. Experiment setup and sample preparation

Data is collected using a 2000W photoexcited infrared thermal imaging system and a portable photoexcited thermal imaging system. The experimental system diagram is shown in Fig. 6. The principle of these two systems is the same, the main difference lies in the use of different light sources as excitation. The high-power system uses two 1 kW halogen lamps to stimulate the specimen on the support at a relatively long distance. The handheld portion of the portable system integrates six 150W halogen lamps and thermal imager. The test piece is excited at close range by controlling software. Two thermal imagers are used in the experiment. Their resolutions were respectively 640×480 and 384×288 respectively. During data acquisition, the sampling frequency is set to 50 Hz.

Seven samples are used for the experiments. Their particulars are shown in Table 3. Samples 1 and 2 are carbon fiber reinforced flat plate composites. They contain internal debonding defects. The diameter, burial depth and distribution of defects are shown in Table 3. Sample 3 is carbon fiber reinforced flexural composite material. The internal debonding defect of the sample is at the bend. Sample 4 is a curved coating material with an aluminum alloy substrate. The buried defect was PVC film of 0.1 mm thickness. Samples 5 and 6 are plate coating samples. The depth of buried defects was 0.6 mm and 0.7 mm, respectively. Sample 7 is rubber pipe test piece. The defect of the sample is the bubble defect at the bond between rubber and pipe.

3.2. Result and analysis

To verify the effectiveness and robustness of the proposed algorithm, four algorithms used for infrared defect detection, one RPCA-based algorithm and two TRPCA-based algorithms are selected for comparison. The four defect detection algorithms include two matrix decomposition

Table 3
Test samples.

Specimen	Indication	Picture
1	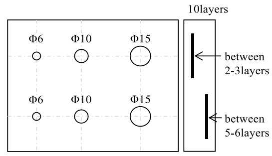	
2	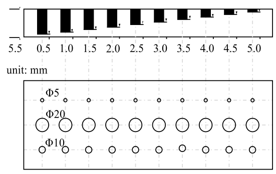	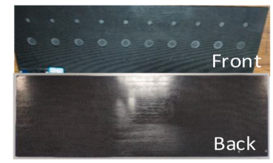
3	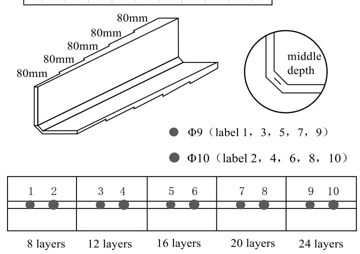	
4	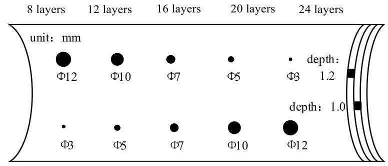	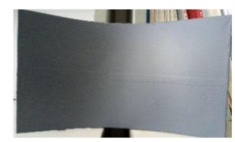
5	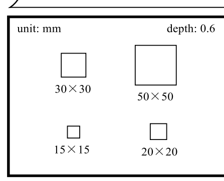	
6	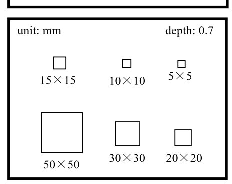	
7	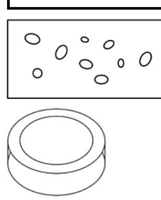	

algorithms (PCA and ICA) and two physical process-based algorithms (PPT and TSR). In PCA algorithm, the first six principal components contain most of the image information. Due to the existence of possible errors, the first seven principal components are selected to retain in order to get the best one. In ICA algorithm, the first eight independent components are retained to select the best one. The RPCA-based algorithm is SIASM. The TRPCA-based algorithms are KBR_TRPCA and IRPRPCA. IRPRPCA and SIASM are used for defect detection. Their sparse components are selected as the final result. Algorithms are processed in MATLAB(R2019a) running on a PC with Windows 10 Professional 64 bits, 2.9 GHz Core Intel(R) CPU i7-10700 and 16 Gb of RAM.

The processing results of each algorithm are shown in Figs. 7–9. Flexural specimen 3, flat coating specimen 6 and rubber pipe specimen 7 were selected for visual display. In the figure, the first row is the result of the four defect detection algorithms, and the second row is the result of the proposed algorithm and the algorithm based on RPCA and TRPCA.

In the results, the detection results of the two algorithms based on TRPCA are noisier. Among them, the detection rate of KBR_TRPCA is lower. In addition, both algorithms have poor interference removal on data with strong light spots. In overall, ICA has the best performance where it has a higher defect detection rate. SIASM has a strong defect detection capability, but it is poor at light spots suppression. Compared with the remaining seven algorithms, the proposed algorithm has the best defect detection performance, which can effectively extract defect features and enhance the display of defects in the thermal image. In terms of defect detection rate, the proposed algorithm can detect more defects. The proposed algorithm also outperforms the rest of the algorithms in detecting defects, especially on data with difficult detection. On data with strong light spots, the proposed algorithm shows better interference removal capability. In the visualization results, the light

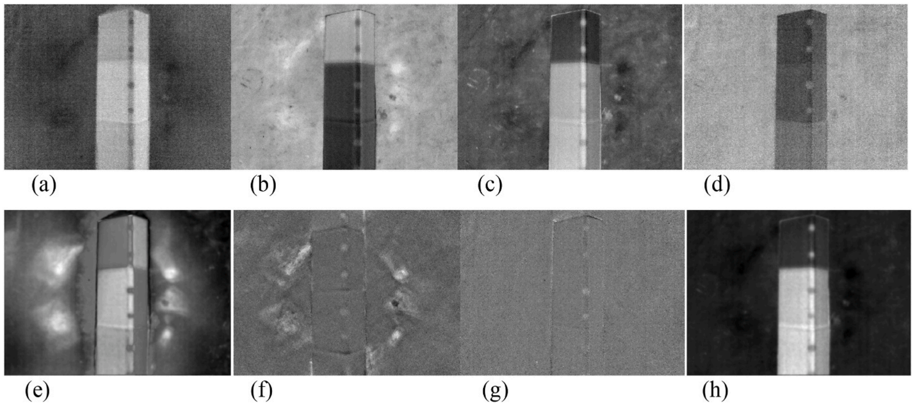

Fig. 7. Images of the detection results of each algorithm for sample 3 (a) PCA. (b) ICA. (c) PPT. (d)TSR. (e)SIASM. (f) IRTRPCA. (g) KBR_TRPCA. (h) Proposed.

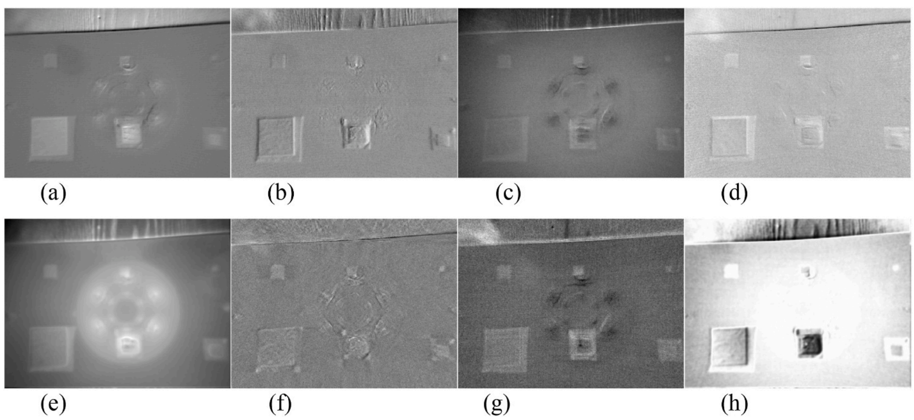

Fig. 8. Images of the detection results of each algorithm for sample 6 (a) PCA. (b) ICA. (c) PPT. (d)TSR. (e)SIASM. (f) IRTRPCA. (g) KBR_TRPCA. (h) Proposed.

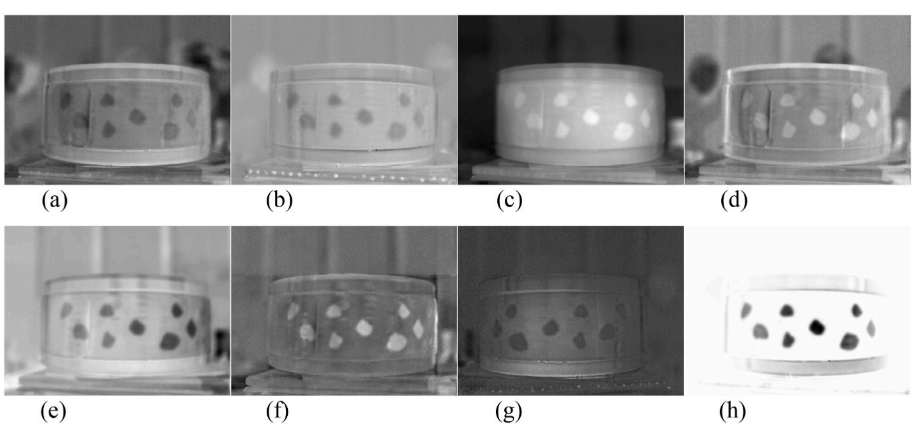

Fig. 9. Images of the detection results of each algorithm for sample 7 (a) PCA. (b) ICA. (c) PPT. (d)TSR. (e)SIASM. (f) IRTRPCA. (g) KBR_TRPCA. (h) Proposed.

spots are also completely suppressed in the results of the proposed algorithm.

For the quantitative analysis, Table 4 gives the F-score and SNR metric values for the results of each algorithm. In the table, the last row is the metrics on average of each algorithm for multiple samples. KBR_TRPCA has the lowest defect detection rate and defect contrast, with F-score and SNR on average of only 0.9 and 1.09 dB respectively. ICA does not have a high SNR, but has the mean F-score of 0.97 and is second only to the proposed algorithm in terms of defect detection rate. Compared to the rest of the algorithms, the proposed algorithm has the highest defect detection rate and defect contrast, with F-score and SNR on average of 1.00 and 3.87 dB respectively. It detects all defects in the sample, and the mean SNR is 2.76 dB higher than the lowest KBR_TRPCA.

Table 5 shows the running time of each algorithm on seven samples. The last row of the table shows the average running time of each algorithm. PCA is the fastest, with the run time of around 1 s. ICA is the next fastest, with an average run time of 1.6 s. TSR and PPT, which are based on physical processes, run inefficiently. The two algorithms of TRPCA are the least efficient. The proposed algorithm is second only to PCA and ICA with an average run time of 5.9 s. For detection tasks where accuracy requirements outweigh efficiency, the run time is within acceptable limits.

Table 4
Performance of different algorithms on F-score and SNR.

sample	indicators	PCA	ICA	PPT	TSR	SIASM	IRT RPCA	KBR_ TRPCA	proposed
1	F-score	0.86	1.00	1.00	1.00	1.00	0.86	0.86	1.00
	SNR	0.31	0.60	0.37	1.65	1.65	0.54	0.68	5.50
2	F-score	0.65	0.89	0.71	0.65	0.77	0.65	0.77	0.94
	SNR	4.89	1.36	2.18	0.98	2.05	1.82	1.33	4.07
3	F-score	0.83	1.00	0.83	1.00	1.00	1.00	0.83	1.00
	SNR	1.49	3.39	2.41	3.05	2.18	1.29	0.81	4.72
4	F-score	1.00	0.90	0.90	0.81	0.81	0.90	0.81	1.00
	SNR	1.69	1.97	2.07	1.56	1.34	2.37	0.87	2.73
5	F-score	1.00	1.00	1.00	1.00	1.00	1.00	1.00	1.00
	SNR	2.30	2.03	5.58	2.08	0.91	2.92	1.16	2.42
6	F-score	1.00	1.00	1.00	1.00	1.00	1.00	1.00	1.00
	SNR	0.93	0.35	0.71	0.44	1.23	0.51	1.88	1.98
7	F-score	1.00	1.00	1.00	1.00	1.00	1.00	1.00	1.00
	SNR	1.61	1.23	1.36	1.79	3.66	2.65	0.94	5.67
Average	F-score	0.91	0.97	0.92	0.92	0.94	0.92	0.90	1.00
	SNR	1.89	1.56	2.09	1.65	1.86	1.72	1.09	3.87

Table 5
Performance of different algorithms on running time.

sample	PCA	ICA	PPT	TSR	SI ASM	IR TRPCA	KBR_ TRPCA	proposed
2	1.2	2.2	65.2	130.5	22	273.8	231.4	7.2
3	0.9	2.1	63.4	128.1	21.5	265.4	210.3	6.5
4	0.8	1.9	59.5	114.5	19.4	254.9	205.2	7.1
5	0.6	1.4	42.6	103.9	15.5	223.5	189.4	6.3
6	0.5	0.9	35.6	82.9	11.2	189.5	145.5	3.8
7	0.5	1.1	39.5	83.5	11.6	190.1	152.3	4.2
11(1)	1.4	2.0	67.8	124.7	15.4	276.5	214.1	6.4
Average	0.8	1.6	53.4	109.7	16.6	239.1	193.3	5.9

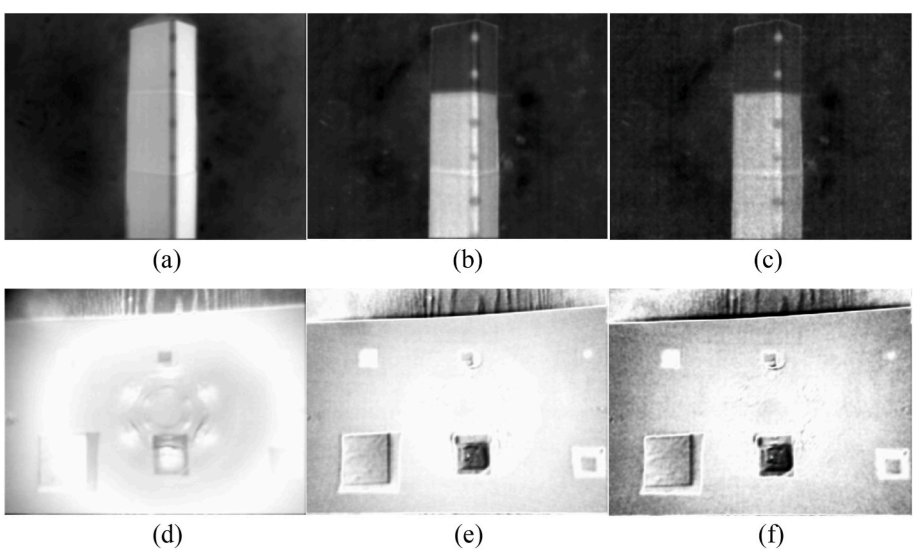

Fig. 10. The resulting images with different rank values (a) sample 3, rank: 1 and 2. (b) sample 3, rank: 1 and 6. (c) sample 3, rank: 1 and 40. (d) sample 6, rank: 1 and 2. (e) sample 6, rank: 1 and 6. (f) sample 6, rank: 1 and 40.

3.3. Parameter setting analysis

In this work, the detection effectiveness of the algorithm is strongly influenced by the selection of the rank. In the defect detection, two ranks were taken as 1 and 6. This was obtained by extensive experimental validation analysis. To illustrate the effect of parameter selection on the algorithm, we have chosen to visualize the detection results for two samples at different values of rank. Fig. 10 show the visualization results for sample 3 and sample 6. Table 6 gives the index values of the detection results for the two samples at different ranks. The results show that the best result images are obtained when the rank values are 1 and 6. When the rank values are similarly low at 1 and 2, the data does not contain enough information, resulting in a background biased image and thus a missed detection. When the rank values are 1 and 40, the higher rank components have more information and contain strong noise, resulting in interference information such as light spots and noise. The resultant component of rank 6 is similar to the first six principal components of PCA. This component contains most of the useful information of the image while also excluding the noisy information contained at higher ranks. Although the resultant images with a larger rank

Table 6
Performance of different rank values.

sample	index	Rank: 1 and 2	Rank: 1 and 6	Rank: 1 and 40
3	F-Score	0.83	1.00	1.00
	SNR	1.27	4.72	4.32
6	F-Score	0.86	1.00	1.00
	SNR	0.48	2.34	2.09

than 6 is similar to the images of rank 6, the choice of 6 as one of the rank values is universal due to computational cost considerations and statistical validation of a large number of experimental results. The resultant images of rank 1 is more like a background image, containing background information with minimal foreground information (defect information). Therefore, rank values of 1 and 6 are reasonable as parameters for the algorithm.

3.4. *Impact of the differential approach on the algorithm*

Partial pattern mismatches caused by direct differencing can affect the extraction of foreground components. Therefore, weights are introduced to reduce the occurrence of mismatched patterns and to further extract defects. This part of the algorithm after the introduction of the weighting component is referred to as the matching difference, whereas without the introduction of the weights it is referred to as the direct difference. In order to illustrate the significance of the existence of matched differences and their impact on the detection performance of the algorithm, the results of two different classes of experimental specimens are selected for specific analysis in this section.

Fig. 11 show the visualization of the detection results for sample 3 and sample 6 under different differential methods, respectively. Table 7 gives the index values of the detection results. For the sample 3, the results show that matched differential has higher defect contrast, clearer defect display and less noise than direct differential detection. For sample 6, matched differencing has a lower defect contrast than direct differencing, while it removes the light spots and noise interference that hinders the observation of defects. In summary, matched differencing can extract more defect information than direct differencing, improve defect contrast and suppress interference such as light spots and noise.

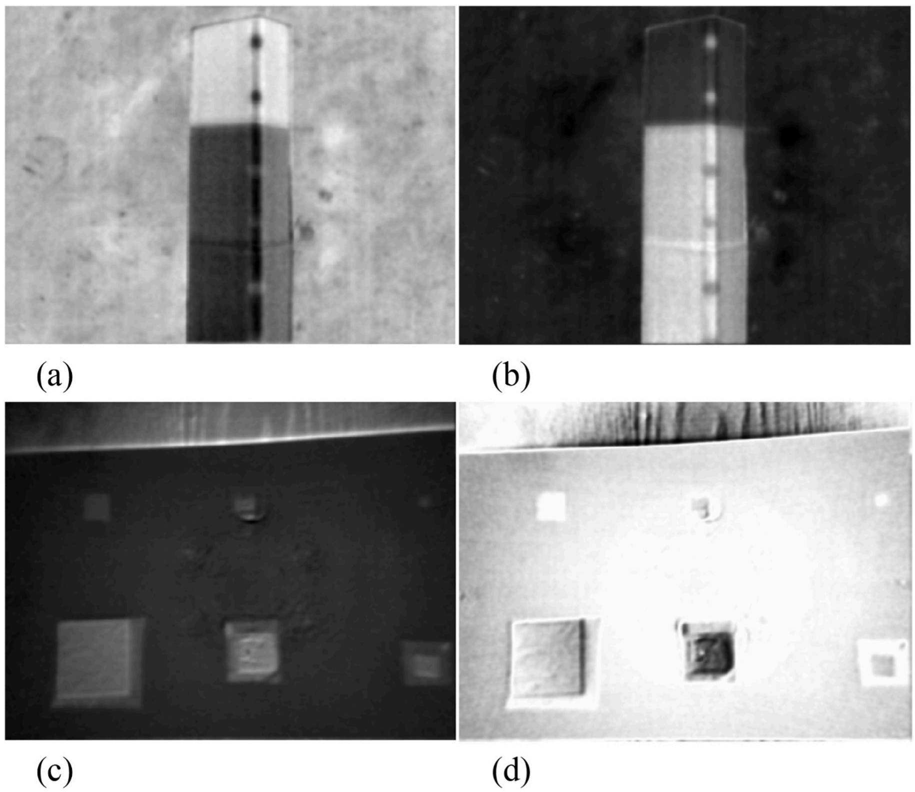

Fig. 11. The resulting images with different differential methods (a) sample 3, direct differencing. (b) sample 3, matched differencing. (c) sample 6, direct differencing. (d) sample 6, matched differencing.

Table 7
Performance of different differential methods.

sample	index	direct differencing	matched differencing
3	F-Score	1.00	1.00
	SNR	4.62	4.72
6	F-Score	1.00	1.00
	SNR	4.48	2.34

4. Conclusion and feature work

This paper proposes a differentiate low rank tensor decomposition algorithm to cope with the detection of defects in complex specimens. The use of tensor rank brings benefit to extract more information of the defects. The probabilistic tensor model corrects for potential mismatch patterns into and achieves defect display enhancement, noise and light spot suppression. Experiments demonstrate that the proposed algorithm achieves the best performance in terms of F-score and SNR metrics for defect detection. n particular, it has excellent performance in non-destructive testing scenarios of composite materials with light spot interference. Future work will focus on the detection of defects arising in the natural environment.

Author statement

Xuran Zhang works and write the main body of the paper, Xuran

Zhang and Bin Gao proposed the new algorithm and do the validation. Tongle Wu, Wai Lok Woo, Junling Fan, Shaozheng Zhan have done the refined work of the paper.

Declaration of competing interest

The authors declare that they have no known competing financial interests or personal relationships that could have appeared to influence the work reported in this paper.

Data availability

Data will be made available on request.

Acknowledgement

The work was supported by National Natural Science Foundation of China (No. 61971093, No. 61527803, No. 61960206010).

References

[1] Li S, Dian R, Fang L, Bioucas-Dias JM. Fusing hyperspectral and multispectral images via coupled sparse tensor factorization. IEEE Trans Image Process Aug. 2018;27(8):4118–30. https://doi.org/10.1109/TIP.2018.2836307.
[2] Qi J, Hu H, Wang Y, Yang C-HH, Marco Siniscalchi S, Lee C-H. Tensor-to-vector regression for multi-channel speech enhancement based on tensor-train network. In: ICASSP 2020 - 2020 IEEE international conference on acoustics, speech and signal processing (ICASSP); 2020. p. 7504–8. https://doi.org/10.1109/ICASSP40776.2020.9052938.
[3] Wang X, Wang W, Yang LT, Liao S, Yin D, Deen MJ. A distributed HOSVD method with its incremental computation for big data in cyber-physical-social systems. In: IEEE transactions on computational social systems, vol. 5; June 2018. p. 481–92. https://doi.org/10.1109/TCSS.2018.2813320. 2.
[4] Zare A, Ozdemir A, Iwen MA, Aviyente S. Extension of PCA to higher order data structures: an introduction to tensors, tensor decompositions, and tensor PCA. In: Proceedings of the IEEE, vol. 106; Aug. 2018. p. 1341–58. https://doi.org/10.1109/JPROC.2018.2848209. 8.
[5] Chachlakis DG, Prater-Bennette A, Markopoulos PP. L1-Norm tucker tensor decomposition. IEEE Access 2019;7:178454–65. https://doi.org/10.1109/ACCESS.2019.2955134.
[6] Haddock J, Kassab L, Kryshchenko A, Needell D. On nonnegative CP tensor decomposition robustness to noise. In: 2020 information theory and applications workshop (ITA); 2020. p. 1–7. https://doi.org/10.1109/ITA50056.2020.9244932.
[7] Liu Y, Long Z, Huang H, Zhu C. Low CP rank and tucker rank tensor completion for estimating missing components in image data. In: IEEE transactions on circuits and systems for video technology, vol. 30; April 2020. p. 944–54. https://doi.org/10.1109/TCSVT.2019.2901311. 4.
[8] Deng X, Jiang P, Peng X, Mi C. An intelligent outlier detection method with one class support tucker machine and genetic algorithm toward big sensor data in internet of things. In: IEEE transactions on industrial electronics, vol. 66; June 2019. p. 4672–83. https://doi.org/10.1109/TIE.2018.2860568. 6.
[9] Hazan T, Polak S, Shashua A. Sparse image coding using a 3D non-negative tensor factorization. In: Tenth IEEE international conference on computer vision (ICCV'05), vol. 1; 2005. p. 50–7. 1.
[10] Veganzones MA, Cohen JE, Cabral Farias R, Chanussot J, Comon P. Nonnegative tensor CP decomposition of hyperspectral data. IEEE Trans Geosci Rem Sens May 2016;54(5):2577–88. https://doi.org/10.1109/TGRS.2015.2503737.
[11] Zhao Q, Zhang L, Cichocki A. Bayesian CP factorization of incomplete tensors with automatic rank determination. IEEE Trans Pattern Anal Mach Intell 2015;37:1751–63.
[12] Lu C, Feng J, Chen Y, Liu W, Lin Z, Yan S. Tensor robust principal component analysis with a new tensor nuclear norm. IEEE Trans Pattern Anal Mach Intell 2020;42:925–38.
[13] Jiang T, Ng MK, Zhao X, Huang T. Framelet representation of tensor nuclear norm for third-order tensor completion. In: IEEE transactions on image processing, vol. 29; 2020. p. 7233–44. https://doi.org/10.1109/TIP.2020.3000349.
[14] Shahid N, Grassi F, Vandergheynst P. Tensor robust PCA on graphs. In: ICASSP 2019 - 2019 IEEE international conference on acoustics, speech and signal processing (ICASSP); 2019. p. 5406–10. https://doi.org/10.1109/ICASSP.2019.8682990.
[15] Zhou P, Feng J. Outlier-robust tensor PCA. In: 2017 IEEE conference on computer vision and pattern recognition (CVPR); 2017. p. 3938–46.
[16] Bengua JA, Phien HN, Tuan HD, Do MN. Efficient tensor completion for color image and video recovery: low-rank tensor train. In: IEEE transactions on image processing, vol. 26; May 2017. p. 2466–79. https://doi.org/10.1109/TIP.2017.2672439. 5.
[17] Cao W, Wang Y, Sun J, Meng D, Yang C, Cichocki A, Xu Z. Total variation regularized tensor RPCA for background subtraction from compressive measurements. IEEE Trans Image Process 2016;25:4075–90.
[18] Peng Y, Meng D, Xu Z, Gao C, Yang Y, Zhang B. Decomposable nonlocal tensor dictionary learning for multispectral image denoising. In: 2014 IEEE conference on computer vision and pattern recognition; 2014. p. 2949–56.
[19] Wu Tongle, Gao Bin, Woo Wai Lok. Hierarchical low-rank and sparse tensor micro defects decomposition by electromagnetic thermography imaging system. Phil. Trans. R. Soc. A 2020;378. 20190584. 20190584.
[20] Tjandra A, Sakti S, Nakamura S. Tensor decomposition for compressing recurrent neural network. In: 2018 international joint conference on neural networks (IJCNN); 2018. p. 1–8. https://doi.org/10.1109/IJCNN.2018.8489213.
[21] Miaoxin L, Xiaoyu Z. Overview of non-destructive testing of composite materials. In: 2020 3rd world conference on mechanical engineering and intelligent manufacturing (WCMEIM); 2020. p. 166–9. https://doi.org/10.1109/WCMEIM52463.2020.00041.
[22] Foudazi A, Edwards CA, Ghasr MT, Donnell KM. Active microwave thermography for defect detection of CFRP-strengthened cement-based materials. IEEE Trans Instrum Meas Nov. 2016;65(11):2612–20. https://doi.org/10.1109/TIM.2016.2596080.
[23] Patryk Kot, Magomed Muradov, Michaela Gkantou, Kamaris George S, Khalid Hashim, David Yeboah. Recent advancements in non-destructive testing techniques for structural health monitoring. Appl Sci 2021;11(6).
[24] Chulkov AO, Vavilov VP. Hardware and software for thermal nondestructive testing of metallic and composite materials. 2016. p. 1392–7.
[25] Farmaki S, Exarchos DA, Tragazikis IK, Matikas TE, Dassios KG. A novel infrared thermography sensing approach for rapid, quantitative assessment of damage in aircraft composites. Sensors 2020;20(15):4113.
[26] Oswald-Tranta B. Time and frequency behaviour in TSR and PPT evaluation for flash thermography. Quantitative InfraRed Thermography Journal 2017;14:164–84.
[27] Maldague X, Marinetti S. Pulse phase infrared thermography. J Appl Phys 1996;79:2694–8.
[28] Rajic N. Principal component thermography for flaw contrast enhancement and flaw depth characterisation in composite structures. Compos Struct 2002;58(4):521–8.
[29] Ishikawa M, et al. Reducing inspection time of pulse phase thermography by using phase data at higher frequency range. Infrared Phys Technol 2018;92:53–9.
[30] Yousefi B, Sfarra S, Ibarra-Castanedo C, Maldague XPV. Comparative analysis on thermal non-destructive testing imagery applying candid covariance-free incremental principal component thermography (CCIPCT). Infrared Phys Technol 2017;85:163–9.
[31] Yousefi B, Castanedo CI, Maldague XPV. Measuring heterogeneous thermal patterns in infrared-based diagnostic systems using sparse low-rank matrix approximation: comparative study. In: IEEE transactions on instrumentation and measurement, vol. 70; 2021. p. 1–9. https://doi.org/10.1109/TIM.2020.3031129. Art no. 4501209.
[32] Liu Yi, et al. Independent component thermography for non-destructive testing of defects in polymer composites. Meas Sci Technol 2019;30(4). 044006-044006.
[33] Wu J, Sfarra S, Yao Y. Sparse principal component thermography for subsurface defect detection in composite products. In: IEEE transactions on industrial informatics, vol. 14; Dec. 2018. p. 5594–600. https://doi.org/10.1109/TII.2018.2817520. 12.
[34] Liu Li, et al. Structured iterative alternating sparse matrix decomposition for thermal imaging diagnostic system. Infrared Phys Technol 2020;107(C).
[35] Chen Y, Cao Z. Change detection of multispectral remote-sensing images using stationary wavelet transforms and integrated active contours. Int J Rem Sens 2013;34:8817–37.
[36] De Lathauwer L, De Moor B, Vandewalle J. A multilinear singular value decomposition. SIAM J Matrix Anal Appl 2000;21:1253–78.